ACS APPLIED MATERIALS & INTERFACES

www.acsami.org

Research Article

Giant Photoluminescence Enhancement and Resonant Charge Transfer in Atomically Thin Two-Dimensional $Cr_2Ge_2Te_6/WS_2$ Heterostructures

Sharidya Rahman, Boqing Liu, Bowen Wang, Yilin Tang, and Yuerui Lu*

Cite This: *ACS Appl. Mater. Interfaces* 2021, 13, 7423−7433

Read Online

ACCESS | Metrics & More | Article Recommendations | Supporting Information

ABSTRACT: Hybridization of two-dimensional (2D) magnetic semiconductors with transition-metal dichalcogenides (TMDC) monolayers can significantly engineer the light−matter interactions and provide a promising platform for enhanced excitonic systems with artificially tailored band alignments. Here, we report the fabrication of heterostructures with monolayer WS_2 on 2D $Cr_2Ge_2Te_6$ (CGT), which displayed giant photoluminescence enhancement at specific CGT layer numbers. The highly enhanced quantum yield obtained can be explained by novel photoexcited carrier dynamics, facilitated by alternate relaxation channels, resulting in resonance charge transfer at the heterointerface. 2D CGT revealed a strongly layer-dependent work function (up to ∼750 meV), which greatly modulates the band positioning in the heterostructure. These heterostructures conceived both type I and type II band alignments, which are verified by Kelvin probe force microscopy and PL measurements. In addition to layer modulation, we uncover temperature and power dependence of the resonance charge transfer in the multilayer heterostructure. Our findings provide further insights into the ultrafast charge dynamics occurring at the atomic interfaces. The results may pave the way for novel optoelectronics based on van der Waals heterostructures.

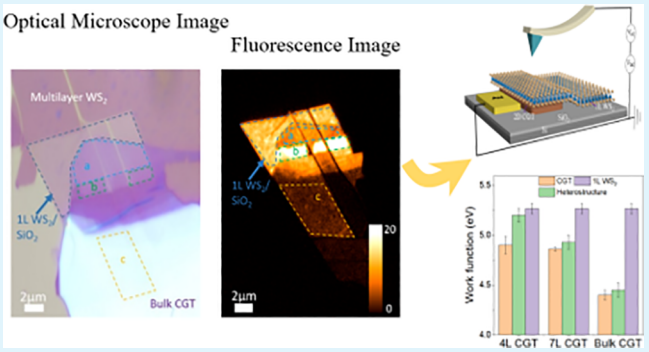

KEYWORDS: *2D heterostructure, interlayer dynamics, quantum yield, KPFM, surface potential*

INTRODUCTION

Research on graphene and consequent two-dimensional materials has attracted immense interest and importance in the last decade.[1−7] Creation of van der Waals (vdW) heterostructures (HSs) from these materials has become an influential strategy to explore new physics[8,9] and new devices such as ultrathin photodetectors[10] and memory devices.[11] This is because HSs expedite the creation of well-defined interfaces through in-plane covalently bonded atomic layers, diminishing the presence of any dangling bonds. Eventually atomically thin layers can be stacked precisely, facilitated by weak vdW interaction between the constituent layers.[8] In addition, the vdW HS does not suffer from the lattice mismatch issue; this minimizes chemical modification and interfacial damage that is desirable for manufacturing clean interfaces for optimal interactions. TMDCs are particularly interesting because of their direct band gap, and atomically sharp interfaces and vdW heterostructures of these semiconducting MX_2 layers have provided seamless possibilities for integration of highly distinct materials at the atomic scale, such as graphene, semimetals, superconductors, and so on. This offers unique platform for various electronic and optoelectronics devices (*e.g.*, transistors, photodetectors, light emitter diodes, and solar cells).[9] However, these materials suffer from low photoluminescence quantum yield (QY), which limits their optoelectronic applications. Monolayer TMDCs are reported to have only 0.01−6% QY,[12] nonradiative recombination centers (for instance due to defect states) being one of the pivotal reasons. In addition, QY is also sensitive to the carrier injection dynamics and relaxation channels.[13]

Recently, another class of materials, $Cr_2X_2Te_6$ (X = Si, Ge, Sn) has emerged as a potential candidate for high-performance nanospintronic application due to their simultaneous inherent ferromagnetic and semiconductor property. They present unique properties and physics, inclusive of valley polarization effects that allow modulation of spin carriers by polarizing light;[14] this paves the way for advancement of valleytronics in data processing. Integration of layered TMDCs with magnetic materials allows sensational engineering of light−matter interactions and pave new avenues for novel electronic,[14,15]

Received: November 10, 2020
Accepted: January 25, 2021
Published: February 4, 2021

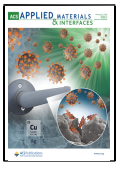

https://dx.doi.org/10.1021/acsami.0c20110
ACS Appl. Mater. Interfaces 2021, 13, 7423−7433

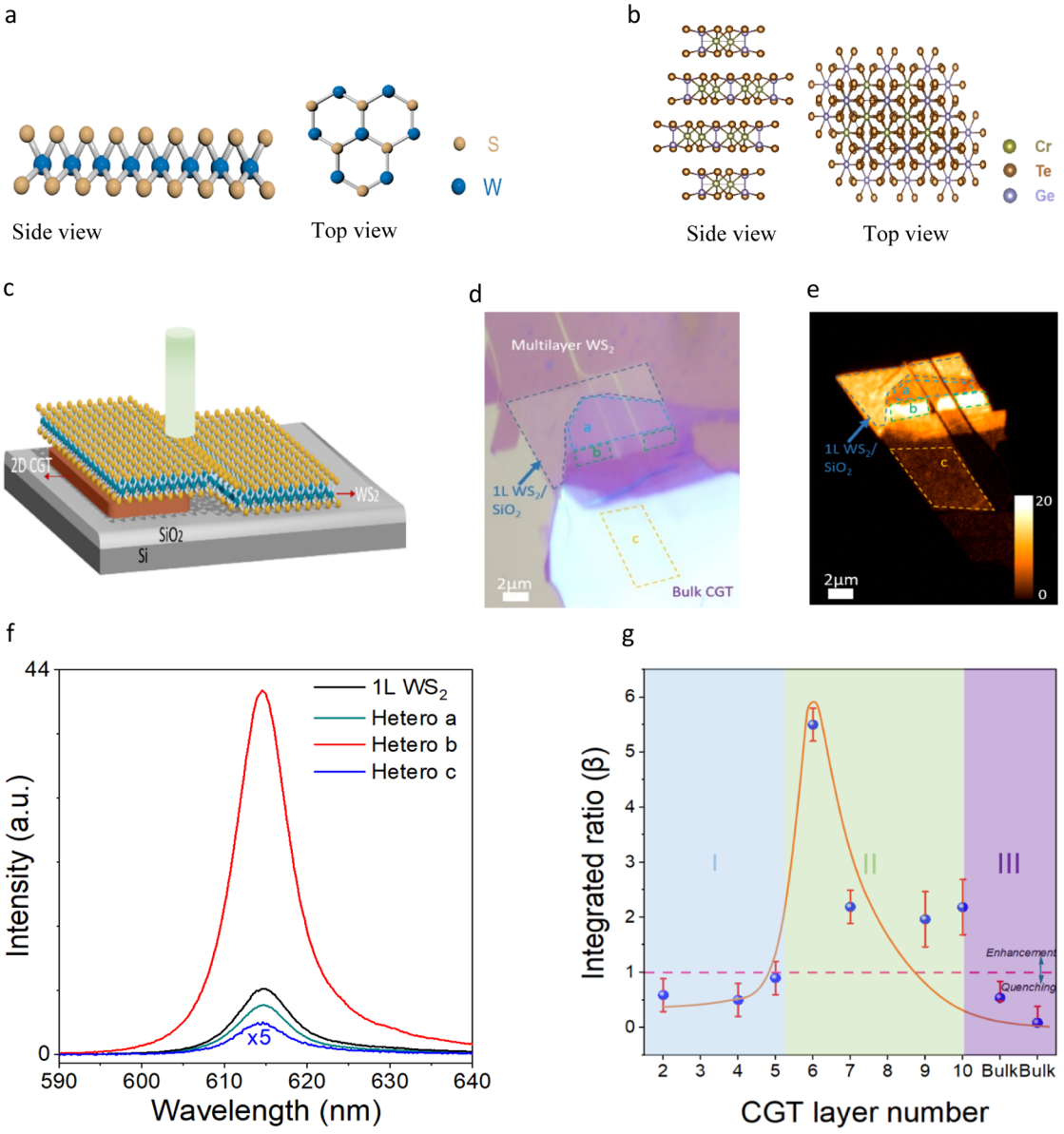

Figure 1. Fabrication and characterization of the heterostructure comprising monolayer WS_2 and 2D CGT. (a) Crystal structure, revealing the side view and top view of WS_2 and (b) 2D CGT. (c) Schematic diagram of the heterostructure showing monolayer WS_2 on 2D CGT supported by the Si/SiO_2 substrate. (d) Optical image of the 1L WS_2/2D CGT heterostructure. Dark-blue dotted lines mark the area of WS_2 only, while sky-blue, green, and orange dotted lines identify the areas for hetero *a* (1L WS_2/4L CGT), hetero *b* (1L WS_2/6L CGT), and hetero *c* (1L WS_2/Bulk CGT). (e) Corresponding fluorescence image of the sample shown in (d). Contrast in brightness clearly reveals the enhancement and quenching in hetero *b* and hetero *a* and *c*, respectively. (f) PL spectra 1L WS_2 and heterostructure *a*, *b*, and *c*. 1L WS_2/6L CGT depicts a massive surge in photoluminescence. (g) Integrated ratio (β) is defined as the ratio of excitons between hetero and 1L WS_2 in the 1L WS_2/CGT heterostructure. Blue balls represent the measured β value as a function of various thicknesses of CGT. Purple dashed line differentiates between quenched and enhanced heterostructure, and the orange line is a guide to the eye. Three identified regions are marked in blue, green, and purple shades. This clearly indicates that enhancement is prominent for certain thickness of CGT, where the resonance charge transfer is dominant.

magnetic,[16] optical/optoelectric,[7,10,17] piezoelectric,[18] magnetoresistive,[19] and superconducting[20] properties. However, there is still limited exploration of their fundamental photophysical characteristics in terms of luminescence properties of heterojunctions containing TMDCs and magnetic 2D materials that can have multifarious applications such as light-emitting devices.[21]

Recent efforts have been manifested for investigating vertical stacks of numerous 2D materials and modulating their unique physical properties.[22−26] In this report, we examine the luminescence characteristics of an unconventional and unique vertical heterostructure consisting of few layers of 2D $Cr_2Ge_2Te_6$ (CGT) and monolayer TMDCs fabricated from mechanical exfoliation and stacking. Heterostructures on various thicknesses of 2D CGT has been analyzed to comprehend the overall phenomena in depth. Fabrication of such atomically thin interfaces between two dissimilar materials reveals extraordinary control of luminescence, unlike any of the magnetic heterostructures reported before, where the layer number of CGT is the most sensitive factor. PL of monolayer WS_2 was modulated by around 2 orders of magnitude (from 33 times PL quenching to 5.5 times PL

https://dx.doi.org/10.1021/acsami.0c20110
ACS Appl. Mater. Interfaces 2021, 13, 7423−7433

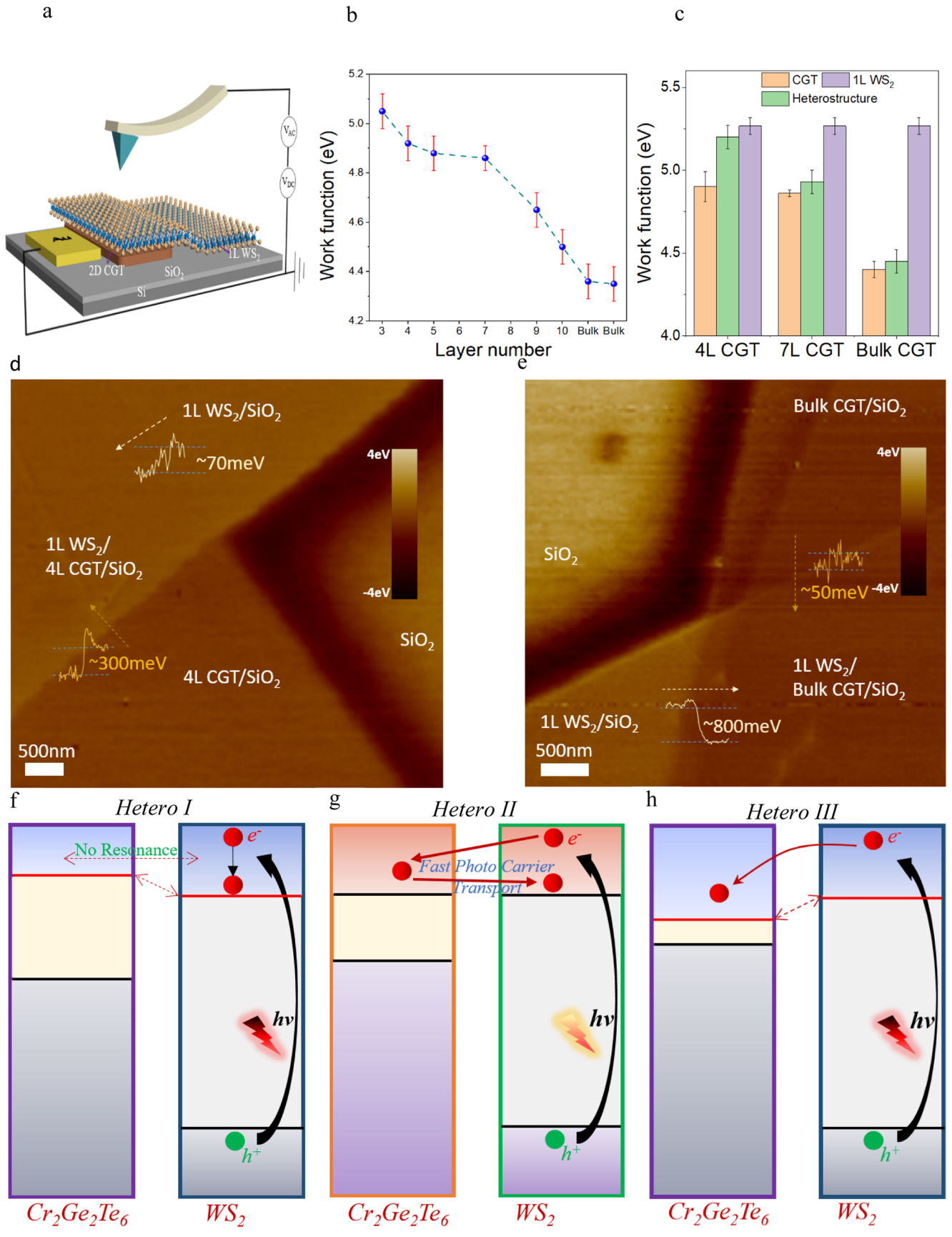

Figure 2. Demonstration of Interlayer charge transfer and measured surface potential of CGT and heterostructure employing Kelvin probe force microscopy (KPFM) (a) Schematic diagram of KPFM measurement. (b) Measured layer-dependent surface potential of CGT. Error bar represents the statistical measurement variations from at least two samples for each thickness of CGT examined. Work function manifests a sharp change with increase in the layer number before becoming constant on reaching bulk layers (c) measured surface potential or work function of CGT, 1L WS_2,

https://dx.doi.org/10.1021/acsami.0c20110
ACS Appl. Mater. Interfaces 2021, 13, 7423−7433

Figure 2. continued

and the heterostructure at room temperature. These are best results from several samples investigated. Work function is represented by the Fermi level (y-axis); Orange bar represents the surface potential of CGT layers; purple bar represents the surface potential of 1L WS_2; green bar represents the work function of the heterostructure, where both the materials have the same Fermi level. Error bar indicates the statistical variations in measurements, averaged through examination of multiple CGT. (d,e) KPFM-measured surface potential image of two typical heterostructure samples showing change in the work function between CGT, WS_2, and the heterostructure. Orange arrow marks the statistical change in potential toward the direction shown at each interface. Monolayer WS_2 renders around ~800meV change in the work function upon contact with bulk CGT (e). Scale bar and color bars are shown in each figures. (f–h) Schematic depiction of the resonance charge transfer mechanism causing the PL surge. Thin CGT layers are able to introduce new excitonic states due to match of the conduction band and hence provide an alternate pathway for hot electron relaxation. In bulk (h) and very thin layer CGT (f), resonance does not takes place due to change in the band gap and misalignment of the conduction band.

enhancement) by altering the thickness of the 2D CGT layer underneath. This high quantum yield was attributed to hot electron relaxation through interlayer hopping using alternate decay channels, leading to rapid charge transfer. Furthermore, long-term emission stability indicated improved resistance to ambient conditions and inconceivability to degradation. To further elucidate the PL enhancement, a powerful Kelvin probe force microscopy (KPFM) tool was used to determine band alignment. 2D CGT illustrated a layer-dependent work function, band gap, and carrier transport, resulting in quantum yield being sensitive to the layer number. In addition to layer alteration, temperature and excitation power were also modulated to validate the existence of resonance charge transfer. Overall plausible reasons for the enhancement have been discussed in compliance with experimental results. Our results pave a new way to engineer the light–matter interaction in atomically thin semiconductors and explore the effect of molecular aggregations in hybrid systems. Furthermore, the vdW ferromagnetic heterostructure provides exceptional opportunity to qualitatively comprehend and regulate band alignment and interfacial coupling, allowing potential applications such as ultrathin lighting diodes, lasers, and so forth. Also, detailed understanding of hot electron dynamics with experimental demonstration is crucial to the design and optimization of devices.

RESULTS AND DISCUSSION

Figure 1a represents the molecular schematic of WS_2 TMDC, which is isostructural and forms a trigonal prismatic frame with six sulfur atoms centered by the tungsten atom.[27] Figure 1b depicts the top view and side view of $Cr_2Ge_2Te_6$. Each crystalline layer forms a honeycomb lattice of $CrTe_6$ shared at the edge, and the central hexagon is dominated by the Ge-dimer. Neighboring layers are bonded by weak van der Waals interactions, allowing easy cleavage of the crystals from bulk down to few layers using mechanical exfoliation.[28,29] This method has been shown to be effective in achieving intact interfaces and ultraclean surfaces and is also an efficient way to avoid contamination.[30] Figure 1c shows the schematic of the heterostructure fabricated from monolayer WS_2 and thin CGT layers (see Methods and supply Figure 1). Consequent to the fabrication, Raman spectroscopy was utilized to characterize and confirm the formation of all heterostructure (refer to Supporting Information, Figure S2, note 1). 2D CGT were characterized by atomic force microscopy (AFM) and phase shifting interferometry (PSI) to confirm the layer number and differentiate between each regions (refer to supply Figures S3–S7 and note 2, Supporting Information); presence of monolayer WS_2 was also confirmed by PSI and Raman spectroscopy (refer to supply Figure S2 and note 1, Supporting Information).[27,30] Figure 1d,e shows the optical image and corresponding fluorescence image of a typical heterostructure sample. Three different hetero (*a*, *b*, and *c*) regions are marked with dotted lines. The fluorescence images clearly indicate variation in the emission intensity, where hetero *b* shows the highest level of emission intensity. Other regions have quenched emissions with varying levels of intensity depending on the thickness of CGT. This indicates the thickness of CGT strongly manipulates the PL emission.

PL spectroscopy is a sensitive and powerful tool to study the dynamics of interlayer and intralayer charge transfer excitonic states.[9,31,32] Figure 1f reveals the room temperature PL spectra of various heterostructures, with primary distinction made in terms of heterostructure *a*, *b*, and *c*. An excitonic peak was observed at around 615 nm (2.01 eV) for 1L WS_2, similar to previous reports,[33] and 5.5 times PL enhancement was perceived in heterostructure *b*. Such observation in PL enhancement is observed multiple times from the same sample and repeatable from three heterostructures fabricated (refer to Figure S8). In contrast, the heterostructure with thinner CGT or bulk CGT renders a quenched PL, where up to 33 times quenching is observed in the PL intensity for bulk CGT/WS_2 hetero. Based on the results, a simple integrated ratio β is defined as the ratio of average PL intensities of the exciton and trion in a heterostructure compared to that of monolayer WS_2, as observed during the experiment (*i.e.*, $\beta = I_{HS}/I_{WS2}$). At RT, only excitons contribute to PL intensity. As witnessed from Figure 1g, the β value changes magnificently with the thickness of CGT, shrinking to 0.03 for the bulk heterostructure and proliferating for heterostructure b, as concluded from the PL report. Interestingly, slight decrease in layer number of CGT causes PL quenching, as witnessed in hetero a; luminescence is found to be altered by an order of magnitude with just few layer difference of CGT. Also, the heterostructure for each region was tested after 3 months of storage in a nitrogen atmosphere and intermittent exposure of air. Heterostructure yielded similar intensity and enhancement, affirming long-term stability (Section III, supply Figure S9, supply note 3, Supporting Information). This result demonstrates that by incorporating WS_2 and 2DCGT in an artificial hierarchical stack, we synthesized materials with consistent optical emission at RT and is also resistant to degradation.

To further emancipate the origin of PL enhancement and determine the band alignment, we directly measure the surface potential of CGT with multiple thicknesses, 1L WS_2 and the heterostructure itself on a Si/SiO_2 substrate, using KPFM (refer to Section IV, supply note 4).[34–36] The measured surface potential of CGT revealed strong layer dependence, while both 1L WS_2 and CGT disclosed massive change in the work function upon forming a heterojunction (Figure 2).

https://dx.doi.org/10.1021/acsami.0c20110
ACS Appl. Mater. Interfaces 2021, 13, 7423–7433

Figure 2a shows schematic for KPFM measurement, where a gold pad was used to make the sample fabricated on the Si/SiO_2 substrate vertically conductive (see Methods). Prior to KPFM measurements, the work function of metal tip (ϕ_{tip}) was calibrated properly and found to be 4.85 eV. Figure 2b shows the tremendous variation of the statistical CGT work function with layer thickness. It ranges from 5.05 ± 0.01 to 4.35 ± 0.01 eV on increasing the thickness of CGT. Bulk layers of CGT possess a similar work function; hence, it stabilizes on reaching a very thick regime. Table 1 and Figure S13 reveal the comparison of the CGT work function variation with conventional TMDCs. WSe_2, WS_2, and MoS_2 depicts only 80 meV, 200 meV, and 400meV variation, respectively,[37−39] when the layer number is regulated from thin toward the bulk regime. CGT manifests 837.5%, 275%, and 87.5% higher potential when compared to each of the TMDCs, respectively. In addition, other members of 2D materials also show miniature modification in relation to CGT; for instance, the CGT portrays 650% and 341.2% higher work function variation compared to graphene and black phosphorus (BP).[34,40] However, it is rather not surprising to observe such tremendous modification of the work function; Yongqing Cai *et al.* predicted large disparity in the work function of BP using first-principles calculations.[41] Such observation may be partly attributed to interlayer screening effect,[42] where the screening length is known to reduce with a higher layer number. Consequently, with the screening effect diminishing with surge of the layer thickness, the surface potential of CGT reaches the intrinsic surface potential of bulk CGT. Furthermore, existence of quantum sizing effect in atomically thin materials may cause thinner CGT layers to have a higher work function, contributing to large variation.[43] Carrier trapping mechanism, local variation in thickness, and environmental adsorbates may affect outcomes of the surface potential,[37] but our relatively uniform KPFM images (Figure 2d,e) undermines these factors. Overall, the intriguing property of CGT can be exploited to implement superior functionality in nanoscale-based devices.

Table 1. Comparison of CGT Work Function with Conventional Materials

	work function variation from a thin layer to bulk regime (meV)	work function variation of CGT as percentage of the conventional material (%)
CGT (this work)	750	
WSe_2[39]	80	837.5
WS_2[38]	200	275
MoS_2[37]	400	87.5
graphene[40]	100	650
BP[34]	170	341.2

Figure 2c−e shows KPFM of two typical heterostructure samples and the statistical summary of different regions (refer to Figure S10 for optical microscope and AFM images). Bulk CGT renders a negative potential between the tip and the sample, leading to smaller a work function, while thinner CGT layers depict positive potential between the sample and tip and lead to higher surface potential values (Figure 2d,e). Figure S12 records the change in the surface potential of 1L WS_2 and 2D CGT with respect to the heterostructure. The average surface potential of WS_2 was found to be 5.3ev, in agreement with the literature value.[35] Monolayer WS_2 samples undergo higher change compared to CGT samples in the heterostructure. As witnessed (Figure 2c−e), the work function of WS_2 decreases by almost 800 meV upon forming a heterojunction with bulk CGT. This variation subsequently dwindles with decrease in the CGT thickness. With 4L CGT, WS_2 undergoes a minor variation (∼70 meV) in its work function. In contrast, CGT samples depict an opposite trend. While bulk CGT experiences negligible variation in the surface potential upon overlapping with WS_2, thinner layers endure a higher deviation; 4L CGT delivers around ∼300 meV difference upon forming the heterostructure. Such interesting results signify strong interaction at the interface, predetermined by the thickness of CGT (refer to Figure S11 for further KPFM characterization). Hence, layer-dependent surface potential of CGT enables modulation and engineering of the exciton dynamics in the CGT/WS_2 heterostructure including generation, dissociation, charge transfer, and recombination that bears ardent importance for fundamental and applied science.

In a heterostructure design with two dissimilar materials, doping behavior is strongly correlated with relative band alignment; hence, it is also crucial to probe the charge transfer, which strongly relies on the work function potential of the semiconductors. Primarily, based on gate-modulated PL measurements, we identify that WS_2 shows slight n-type behavior (refer to Section V, Note 5, Figure S14, Supporting Information), while FET characterization of CGT complies with p-type behavior (refer to Section V, supply note 6, Figure S15, Supporting Information). WS_2 has been shown to be of n-type in previous reports,[44] and due to slight n-doping observed in our results, it is assumed that the Fermi level of 1L WS_2 is positioned slightly above the intrinsic level before contact (refer to Figure S16). While for CGT, Fermi is positioned below the middle of the band gap. P-type behavior of CGT is consistent with previous results.[45,46] Figure 2f−h shows the schematic of three possible scenarios occurring in different heterostructures. Resonance charge transfer phenomena occurring in hetero II cause the PL enhancement (Figure 2g). It can be hypothesized that, when the Fermi levels align after contact, the energy level of conduction bands would also align for both CGT and WS_2, resulting in ultrafast charge redistribution at the interface on photoexcitation. Photoinduced excitations with high energy photons ($h\nu$ > band gap of WS_2) results in a pair of electron (e^-) and hole (h^+); this energetic electron is able to transfer from WS_2 to the CGT side first and move back to WS_2 again for hetero II; this interfacial electron transfer takes place in the femtosecond region[47] before relaxation; hot photoelectrons can lose their excess energy very rapidly due to electron−phonon and electron−electron interaction. Phonon vibrations are known to alleviate charge relocation, and electron−phonon interactions are responsible for providing crucial channels for hot electron relaxation.[47] Therefore, quantum efficiency is significantly enhanced, causing rapid surge of photoluminescence in 1L WS_2 when combined with six-layer CGT. CGT is able to introduce additional excitonic states and furnish alternate pathways for interlayer electron hopping and relaxation. It has been reported earlier that near-resonant excitation of excitonic states is able to increase the quantum efficiency due to efficient carrier relaxation.[48] Six-layer CGT causes similar effects by introducing new pathways for carrier recombination; it is clear that the large offset in the valence band imposes a massive barrier in carrier injection;[49] holes are unable to disseminate

https://dx.doi.org/10.1021/acsami.0c20110
ACS Appl. Mater. Interfaces 2021, 13, 7423−7433

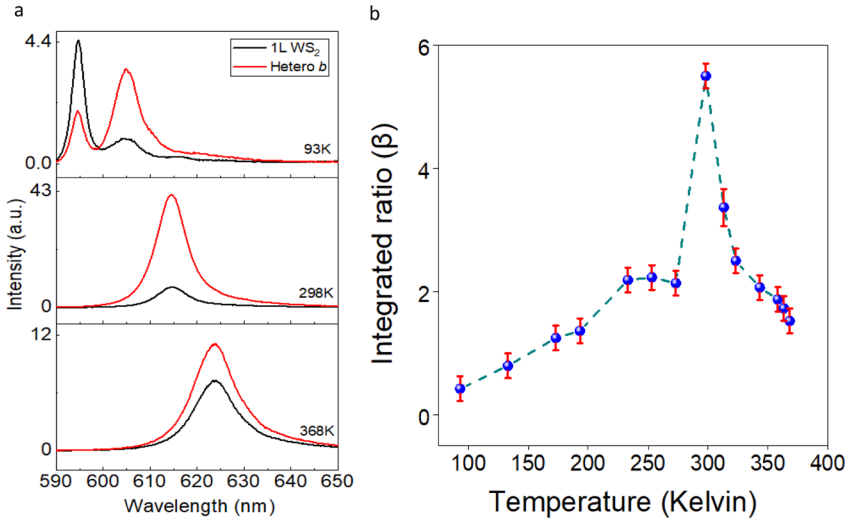

Figure 3. Temperature dependence of resonance charge transfer: (a) PL spectrum of 1L WS_2 and hetero *b* as a function of temperature. The black and red solid lines denote the experimental data from the 1L WS_2 and heterostructure, respectively. (b) Integrated ratio, β, as a function of temperature in hetero *b* (1L WS_2/6L CGT). The blue ball represents the measured β value as a function of temperature. It suggests the charge transfer is dominant only when the resonance takes place at RT, giving the maximum enhancement. Resonance is lost on increasing or decreasing the temperature.

and flow from WS_2 to CGT and further contribute in the recombination process. This possible mechanism along with strong interface coupling sheds considerable light on the origin of PL enhancement in hetero *b*. The interference effect on PL modulation can easily be excluded (refer to supply note 7, Supporting Information). The resonance condition is however absent in hetero I, and hence, there is no increment in photoluminescence (Figure 2f). In these cases, photoexcited electrons are expected to relax in on larger time scale without any redistribution, as shown schematically in Figure 2f.

Some recent studies have reported a similar process of hot carrier relaxation in molecular semiconductor interfaces and chemically synthesized quantum dots.[47,50−52] Zhang *et al.* hypothesized a novel interlayer hopping mechanism using realistic DFT simulation on a $MoSe_2/WSe_2$ bilayer system.[47] Existence of an identical pathway was also confirmed by Tisdale *et al.* in semiconductor nanocrystal PdSe on bulk TiO_2.[50] Forward and reverse hole transfer have been examined by Chu *et al.* between TiO_2 and Ch_3OH,[51] while Chen *et al.* experimentally reassured reverse hole transfer occurring within few hundred femtoseconds in a photoexcited methanol carbon nitride system.[52] Pump and probe spectroscopy also has proven ultrafast carrier movement.[9] It can also be speculated that quantum efficiency can be further ameliorated through creation of additional electron−hole pairs by the carrier multiplication process.[53]

According to literature,[28] the band gap of CGTincreases with decrease in thickness, with the highest reaching 0.86 eV in the monolayer.[54] Figure S16 shows the measured possible band alignment occurring before and after contact for three different regions. Thinner CGT layers (4L and below) are likely to form type II heterojunction, as measured by KPFM due to contact doping; a larger band gap of CGT could account for the change in band alignment, resulting in the charge distribution. However, due to restriction of hole movement caused by the large valence band offset, only electrons are transferred to the WS_2 side, causing further n-doping and leading to PL quenching. This is also consistent with spontaneous photoinduced transfer of charge and creation of interlayer excitons.[55] Although the interlayer relaxation process at band edge competes with the alternate relaxation pathway, namely, the intralayer relaxation, but the former process has been illustrated to be significantly faster; interlayer transitions occur in the femtosecond regime, while intralayer transition would be in the picosecond range[55] and cause intralayer recombination in a heterostructure that would be similar to monolayer standing alone. Here, photocarrier dynamics is not prominent since there is significant mismatch between the conduction band and no resonance takes place (Figure 2f). In contrast, hetero b symbolizes ardent competition between contact doping and photocarrier dynamics. It is reasonable to expect PL quenching by roughly 3.6 times due to contact doping (estimated from Figure S16b), but a more dominant mechanism of hot electrons relaxation leads to around 5.5 times of enhancement in emission intensity. Therefore, the photocarrier doping manifests around ∼16 fold effective increment in PL, crafting exciting application for light-harvesting devices. For bulk CGT layers, band gap is very small and KPFM measurements leads to type I before and after measurements. Contact doping in this case is immensely massive, causing almost ∼800meV change in the doping level (Figure 2c,e). In addition, conduction band offset and inbuilt potential of CGT and WS_2 is relatively large, resulting in a large proportion of photoexcited electrons being transferred from WS_2 to the CGT layer (Figure 2h). Similarly, a large band offset between the valence band of CGT and WS_2 restricts the movement of holes. This advocates for the large quenching in photoluminescence of WS_2 in hetero III. It is may be reasonable for one to expect excitons in the CGT layer upon transferring of electrons, but CGT is an indirect band gap semiconductor[46] and the quantum yield of exciton emission would be very low. Furthermore, the possible exciton emission from the CGT layer is predicted to be in the energy range of 0.23ev to 0.85ev, which is much beyond our detector range.

Considering the model is assertive, PL enhancement is then directly regulated by the resonance and interface dynamics. Therefore, if the process is somehow disrupted, then resonance would be removed and the increment in the emission intensity

https://dx.doi.org/10.1021/acsami.0c20110
ACS Appl. Mater. Interfaces 2021, 13, 7423−7433

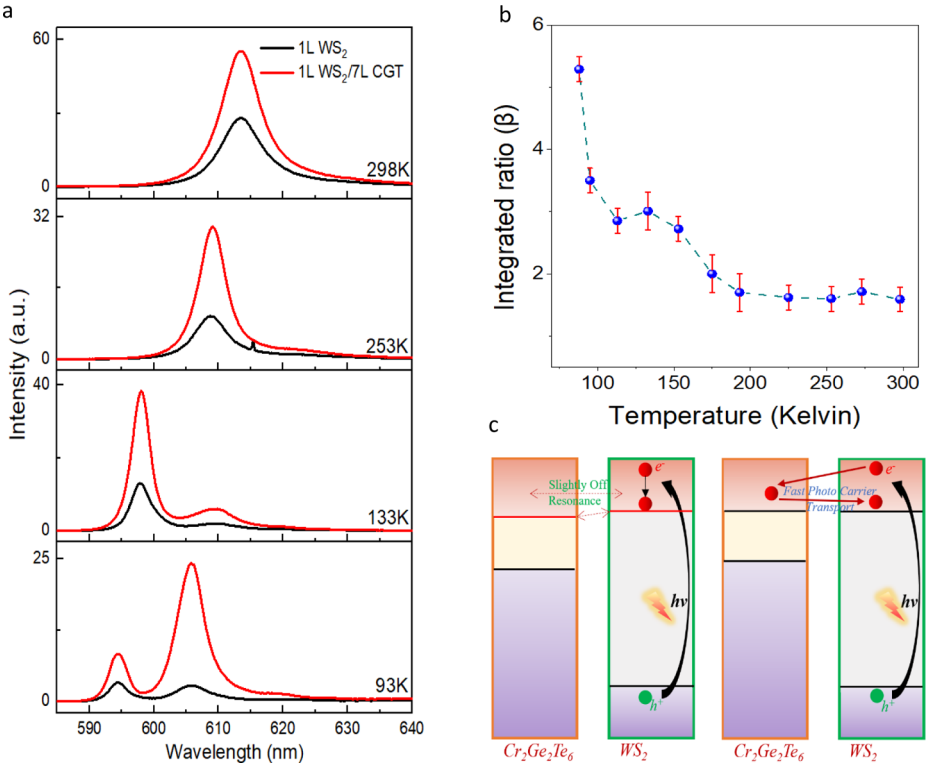

Figure 4. Layer-dependent modulation of resonance charge transfer: (a) Temperature-dependent PL spectrum of 1L WS_2 and 7L CGT showing resonance PL enhancement at low T. The black and red solid lines denote the experimental data from the 1L WS_2 and heterostructure, respectively. (b) Integrated ratio, β, as a function of temperature in 1L WS_2/7L CGT. The blue ball represents measured β value as a function of temperature. It suggests the charge transfer is disrupted by changing the layer number at RT and is dominant again only when the resonance takes place at low T due to matching of conduction band, giving the maximum enhancement. Resonance is lost on changing the temperature, hence reducing the ratio β. (c) Schematic illustration of charge transfer phenomena due to temperature modulation in 1L WS_2/7L CGT. Misalignment of excitonic states in RT disengages the resonance charge transfer. Tuning the temperature to a lower range can re-engage the phenomena and increase the PL quantum yield.

would decline and disappear. It becomes imperative to scrutinize further and emancipate the existence of this elusive phenomena. Therefore, we study the luminescence property by sweeping the temperature to deepen the understanding of interface coupling and dynamics. Figure 3a,b shows the temperature-dependent PL measurements and ratio β of hetero *b*. The average of integrated PL areas of 1L WS_2 and hetero *b* is shown in supply Figure S17. Enhancement gradually decreases upon either increasing or decreasing the temperature, indicating the resonance is lost; this is because the temperature changes the Fermi level.[56,57] On decreasing the temperature from RT, the Fermi level of WS_2 moves toward the conduction band, while that of CGT shifts toward the valence band. Realignment of the Fermi level causes contact doping again, resulting in a slight offset in the conduction band. Hence, resonant movement of electrons is disrupted, which reduces the quantum yield and enhancement factor to decrease rapidly, suggesting a disruption to the ultrafast electron dynamics occurring previously. On further decreasing the temperature, the significant change in the Fermi level completely withers off the band alignment to typical type II, causing further n-doping of WS_2 and PL quenching (Figure S18). Same observations are noted upon increasing the temperature beyond RT. However, Fermi levels of the constituent material move in the opposite direction due to thermal injection of electrons, establishing the contact doping. Detuning of the resonant charge transfer leads to type I alignment and decrement in quantum yield; this accounts for the gradual decrease in ratio β. This validates our model to a greater certainty. Nonradiative recombination center-like defect-mediated traps could also account for PL reduction.[58] To our surprise, it has been observed that lowering the temperature causes 3 orders of magnitude increase in charged exciton emission. Figure 3a indicates at 93 K, 1L WS_2 has higher exciton emission at ~595 nm, but a lower trion emission at 605 nm. A trion is formed when either an electron or hole binds to an exciton. Therefore, at low temperature, contact doping from CGT assimilates a higher trion to exciton ratio, which confirms the band alignment and KPFM measurements. Rise in electron densities[59] and unintentional doping by CGT could also increase the likelihood for the exciton to interact with the electron reservoir and bind to the trion. This enhances the trion population, as observed in photoexcited hetero *b*. Effects of augmenting the excitation power (refer to Section VII, supply note 8) is shown in Figure S19, which further clarifies the intriguing decay process.

In addition to temperature modulation, another way to manipulate the photoinduced mechanism would be by altering the work function of CGT and monitor the resonance effect. 7L CGT has a lower work function at RT, so it does not entirely resonate, but the conduction band offset with WS_2 is very modest. Hence, it can be predicted that modulating the temperature for 7L CGT and monolayer WS_2 hetero would trigger the Fermi level and activate resonance at low temperature; similarly, PL enhancement would be perceived with surplus quantum yield. To elucidate our hypothesis, we

https://dx.doi.org/10.1021/acsami.0c20110
ACS Appl. Mater. Interfaces 2021, 13, 7423−7433

investigate the luminescence features for the 1L WS_2/7L CGT heterostructure; Figure 4a,b shows the overall report (refer to supply Figure S20 for average Pl areas). Maximum enhancement is only observed at low temperature, indicating the resonance is only evident when the conduction band aligns and new electron pathways are introduced. At RT, the band gap of 7L CGT is slightly lower than that of 6L CGT, which results in mismatch in the conduction band level. Decreasing the temperature administers further p-type and n-type doping in CGT and WS_2, respectively; hence, the resulting contact doping re-establishes resonant condition with new decay channels and augments the quantum yield. The integrated ratio β obtained at low temperature for the 7L CGT heterostructure is similar to that of 6L CGT hetero at RT, shedding further insights on existence of novel hot-carrier dynamics. The entire process is schematically depicted in Figure 4c.

From our modeling of the TMDC/2D CGT heterostructure, we deduce that cooperative and more plausible explanation of the RT PL enhancement can be attributed to strong interaction at the interface and introduction of new excitonic states. In a multilayer system,[25] this can be effective in introducing new radiative decay channels. Large variation in the CGT work function with the layer number is able to cause such variation in band alignment in the heterostructure and hence give rise to unique decay routes. PL enhancement can also be manifested by the reduction in defect centers that magnificently increases the quantum efficiency of the emission. It is anticipated and speculated that further detailed theoretical and simulation studies supported by relevant experimental demonstrations can disclose the electronic and molecular structure of the interface between WS_2 and CGT; this will contribute to the PL enhancement investigated in this work.[60,61]

In summary, 2D CGT and TMDCs have been recognized as convincing materials for optoelectronic applications. While defect states in TMDCs may illustrate poor emission, 2D CGT also suffers from air instability over a long period of exposure when layer numbers are thinned down.[62] By coupling the two materials in a vertical heterostructure, large enhancement has been observed in photoemission in comparison with bare TMDCs; in addition, the heterostructure is stable over a long period, expanding its application. PL enhancement is of 5.5 order magnitude at room temperature. Definitely, further understanding of the interface structure is required to better explain the elusive phenomena observed in our results. However, giant PL enhancement with extended air stability under ambient condition projects several prospects of practical applications for the WS_2/CGT heterostructure in high-efficiency solar cells, photovoltaics, lasers, and optoelectronic devices.

METHODS

Device Fabrication and Characterization. 2D flakes of CGT and monolayer WS_2 were prepared by the well-proven mechanical exfoliation method.[63] The Si/SiO_2 wafers were at first cut into 10 × 10 mm^2-size chips; this was followed by thorough cleaning in an ultrasonic bath of acetone, IPA, and DI water in sequence. CGT tapes were directly put into the substrate and baked or annealed on a hot plate for 2 min at ∼100 C. The heating step has been used previously by other researchers to obtain large-area graphene previously.[63,64] 2D CGT flakes were consequently transferred onto the substrate after the tape had been withdrawn on cooling. The flakes were then identified by an ultrahigh resolution optical microscope from Nikon. Monolayer WS_2 was similarly exfoliated by the Scotch tape method, but the tape was put onto a viscoelastic PDMS stamp; the monolayer was identified through optical contrast and microscope fluorescence imaging. It was then transferred on top of designated CGT flakes *via* the dry transfer method[65] to form the heterostructure (see Figure S1 for details of transfer method). Both the crystals (CGT and WS_2) are from same batch obtained commercially from HQ Graphene. A MOS device was used for gate-dependent PL measurement of WS_2. A gold electrode with a thickness of 100 nm was used as a probing pad; it was transferred mechanically to partially make contact with the WS_2 flake.

Optical Characterization. A Horiba LabRAM system equipped with a confocal microscope, a charge-coupled device Si detector, and a 532 nm diode-pumped solid state laser as the excitation source was deployed for conducting PL and Raman measurements. An objective lens was used to focus the laser light on the surface of the sample. The illuminated spot on the samples is estimated to have a diameter of ∼2 μm. The spectral response of the entire system was determined with a calibrated halogen-tungsten light source. For temperature-dependent measurements, the sample was placed on a microscope compatible Linkam chamber connected to a temperature controller; liquid nitrogen was used as the coolant. For gate-dependent measurements, a Keithley 4200 semiconductor analyzer was utilized for application of electrical bias. Instrument response was deducted from all Pl spectras. All optical path length measurements were obtained using a phase-shifting interferometer (Veeco NT9100).

KPFM Characterization. The gold electrodes were prepatterned on a Si/SiO_2 substrate (275 nm thermal-doped n± doped silicon) by conventional photolithography, metal deposition, and lift-off processes. Dry transfer (described above) was used to transfer flakes to be in contact with Au electrodes. KPFM was applied to compute the surface potential. The KPFM model used in the experiments was Bruker MultiMode VIII with Peak Force TUNA.

ASSOCIATED CONTENT

Supporting Information

The Supporting Information is available free of charge at https://pubs.acs.org/doi/10.1021/acsami.0c20110.

Sample fabrication and identification, PSI and AFM characterization, long-term stability, KPFM characterization, determination of doping levels in WS_2 and CGT and measured band alignment, and power-dependent analysis (PDF)

AUTHOR INFORMATION

Corresponding Author

Yuerui Lu − *Research School of Electrical, Energy and Materials Engineering, College of Engineering and Computer Science, The Australian National University, Canberra 2601, Australia;* orcid.org/0000-0001-6131-3906; Email: yuerui.lu@anu.edu.au

Authors

Sharidya Rahman − *Research School of Electrical, Energy and Materials Engineering, College of Engineering and Computer Science, The Australian National University, Canberra 2601, Australia;* orcid.org/0000-0002-2195-0406

Boqing Liu − *Research School of Electrical, Energy and Materials Engineering, College of Engineering and Computer Science, The Australian National University, Canberra 2601, Australia*

Bowen Wang − *Research School of Electrical, Energy and Materials Engineering, College of Engineering and Computer Science, The Australian National University, Canberra 2601, Australia*

Yilin Tang − *Research School of Electrical, Energy and Materials Engineering, College of Engineering and Computer*

https://dx.doi.org/10.1021/acsami.0c20110
ACS Appl. Mater. Interfaces 2021, 13, 7423−7433

Science, The Australian National University, Canberra 2601, Australia

Complete contact information is available at: https://pubs.acs.org/10.1021/acsami.0c20110

Author Contributions

Y.L. supervised the project. S.R. fabricated the samples and conducted all PL and PSI measurements. B.L. contributed to AFM and KPFM measurements. B.W. contributed to MOS device fabrication. S.R. analyzed and interprated all data and wrote the manuscript.

Notes

The authors declare no competing financial interest.

■ ACKNOWLEDGMENTS

Authors acknowledge Professor Daniel Macdonald and Dr Hieu Ngyuen from the Australian National University for their facility support. We would like to acknowledge the financial support from ANU PhD student scholarship, Australian Research Council, ANU Major Equipment Committee fund (14MEC34), National Natural Science Foundation of China, Australian Research Council (ARC), Discovery Early Career Researcher Award (DECRA) (DE140100805), ARC Discovery Project (DP180103238), and Australian National Heart Foundation (ARIES ID: 35852).

■ REFERENCES

(1) Castro Neto, A. H.; Guinea, F.; Peres, N. M. R.; Novoselov, K. S.; Geim, A. K. The Electronic Properties of Graphene. *Rev. Mod. Phys.* **2009**, *81*, 109−162.

(2) Butler, S. Z.; Hollen, S. M.; Cao, L.; Cui, Y.; Gupta, J. A.; Gutiérrez, H. R.; Heinz, T. F.; Hong, S. S.; Huang, J.; Ismach, A. F.; Johnston-Halperin, E.; Kuno, M.; Plashnitsa, V. V.; Robinson, R. D.; Ruoff, R. S.; Salahuddin, S.; Shan, J.; Shi, L.; Spencer, M. G.; Terrones, M.; Windl, W.; Goldberger, J. E. Progress, Challenges, and Opportunities in Two-Dimensional Materials Beyond Graphene. *ACS Nano* **2013**, *7*, 2898−2926.

(3) Li, L.; Yu, Y.; Ye, G. J.; Ge, Q.; Ou, X.; Wu, H.; Feng, D.; Chen, X. H.; Zhang, Y. Black Phosphorus Field-effect Transistors. *Nat. Nanotechnol.* **2014**, *9*, 372.

(4) Palacios-Berraquero, C.; Barbone, M.; Kara, D. M.; Chen, X.; Goykhman, I.; Yoon, D.; Ott, A. K.; Beitner, J.; Watanabe, K.; Taniguchi, T.; Ferrari, A. C.; Atatüre, M. Atomically Thin Quantum Light-Emitting Diodes. *Nat. Commun.* **2016**, *7*, 12978.

(5) Palacios-Berraquero, C.; Kara, D. M.; Montblanch, A. R. P.; Barbone, M.; Latawiec, P.; Yoon, D.; Ott, A. K.; Loncar, M.; Ferrari, A. C.; Atatüre, M. Large-Scale Quantum-Emitter Arrays in Atomically Thin Semiconductors. *Nat. Commun.* **2017**, *8*, 15093.

(6) Saito, Y.; Nakamura, Y.; Bahramy, M. S.; Kohama, Y.; Ye, J.; Kasahara, Y.; Nakagawa, Y.; Onga, M.; Tokunaga, M.; Nojima, T.; Yanase, Y.; Iwasa, Y. Superconductivity Protected by Spin−Valley Locking in Ion-Gated MoS_2. *Nat. Phys.* **2015**, *12*, 144.

(7) Wang, Q. H.; Kalantar-Zadeh, K.; Kis, A.; Coleman, J. N.; Strano, M. S. Electronics and Optoelectronics of two-dimensional Transition Metal Dichalcogenides. *Nat. Nanotechnol.* **2012**, *7*, 699.

(8) Geim, A. K.; Grigorieva, I. V. Van der Waals Heterostructures. *Nature* **2013**, *499*, 419.

(9) Hong, X.; Kim, J.; Shi, S.-F.; Zhang, Y.; Jin, C.; Sun, Y.; Tongay, S.; Wu, J.; Zhang, Y.; Wang, F. Ultrafast Charge Transfer in Atomically thin MoS_2/WS_2 Heterostructures. *Nat. Nanotechnol.* **2014**, *9*, 682.

(10) Britnell, L.; Ribeiro, R. M.; Eckmann, A.; Jalil, R.; Belle, B. D.; Mishchenko, A.; Kim, Y. J.; Gorbachev, R. V.; Georgiou, T.; Morozov, S. V.; Grigorenko, A. N.; Geim, A. K.; Casiraghi, C.; Neto, A. H. C.; Novoselov, K. S. Strong Light-Matter Interactions in Heterostructures of Atomically Thin Films. *Science (Washington, DC, U.S.)* **2013**, *340*, 1311.

(11) Sup Choi, M.; Lee, G.-H.; Yu, Y.-J.; Lee, D.-Y.; Hwan Lee, S.; Kim, P.; Hone, J.; Jong Yoo, W. Controlled Charge Trapping by Molybdenum Disulphide and Graphene in Ultrathin Heterostructured Memory Devices. *Nat. Commun.* **2013**, *4*, 1624.

(12) Jie, W.; Yang, Z.; Bai, G.; Hao, J. Luminescence in 2D Materials and Van Der Waals Heterostructures. *Adv. Opt. Mater.* **2018**, *6*, 1701296.

(13) Kozawa, D.; Kumar, R.; Carvalho, A.; Kumar Amara, K.; Zhao, W.; Wang, S.; Toh, M.; Ribeiro, R. M.; Castro Neto, A. H.; Matsuda, K.; Eda, G. Photocarrier Relaxation Pathway in two-dimensional Semiconducting Transition Metal Dichalcogenides. *Nat. Commun.* **2014**, *5*, 4543.

(14) Mak, K. F.; Lee, C.; Hone, J.; Shan, J.; Heinz, T. F. Atomically Thin MoS_2: A New Direct-Gap Semiconductor. *Phys. Rev. Lett.* **2010**, *105*, 136805.

(15) Lee, C.-H.; Lee, G.-H.; van der Zande, A. M.; Chen, W.; Li, Y.; Han, M.; Cui, X.; Arefe, G.; Nuckolls, C.; Heinz, T. F.; Guo, J.; Hone, J.; Kim, P. Atomically Thin p−n junctions with Van der Waals Heterointerfaces. *Nat. Nanotechnol.* **2014**, *9*, 676.

(16) Xu, X.; Yao, W.; Xiao, D.; Heinz, T. F. Spin and Pseudospins in Layered Transition Metal Dichalcogenides. *Nat. Phys.* **2014**, *10*, 343.

(17) Ross, J. S.; Klement, P.; Jones, A. M.; Ghimire, N. J.; Yan, J.; Mandrus, D. G.; Taniguchi, T.; Watanabe, K.; Kitamura, K.; Yao, W.; Cobden, D. H.; Xu, X. Electrically Tunable Excitonic Light-emitting Diodes based on Monolayer WSe_2 p−n junctions. *Nat. Nanotechnol.* **2014**, *9*, 268.

(18) Wu, W.; Wang, L.; Li, Y.; Zhang, F.; Lin, L.; Niu, S.; Chenet, D.; Zhang, X.; Hao, Y.; Heinz, T. F.; Hone, J.; Wang, Z. L. Piezoelectricity of Single-Atomic-layer MoS_2 for Energy Conversion and Piezotronics. *Nature* **2014**, *514*, 470.

(19) Ali, M. N.; Xiong, J.; Flynn, S.; Tao, J.; Gibson, Q. D.; Schoop, L. M.; Liang, T.; Haldolaarachchige, N.; Hirschberger, M.; Ong, N. P.; Cava, R. J. Large, Non-Saturating Magnetoresistance in WTe_2. *Nature* **2014**, *514*, 205−208.

(20) Morosan, E.; Zandbergen, H. W.; Dennis, B. S.; Bos, J. W. G.; Onose, Y.; Klimczuk, T.; Ramirez, A. P.; Ong, N. P.; Cava, R. J. Superconductivity in Cu_xTiSe_2. *Nat. Phys.* **2006**, *2*, 544−550.

(21) Andrzejewski, D.; Hopmann, E.; John, M.; Kümmell, T.; Bacher, G. WS_2 Monolayer-based Light-Emitting Devices in a Vertical p−n Architecture. *Nanoscale* **2019**, *11*, 8372−8379.

(22) Jin, C.; Ma, E. Y.; Karni, O.; Regan, E. C.; Wang, F.; Heinz, T. F. Ultrafast Dynamics in Van der Waals Heterostructures. *Nat. Nanotechnol.* **2018**, *13*, 994−1003.

(23) Petoukhoff, C. E.; Voiry, D.; Bozkurt, I.; Chhowalla, M.; Dani, K. M. *Probing Charge Transfer States in Polymer:Fullerene − MoS_2 Van der Waals Heterostructures, Conference on Lasers and Electro-Optics, San Jose, California, 2018/05/13*; Optical Society of America: San Jose, California, 2018.

(24) Zhong, D.; Seyler, K. L.; Linpeng, X.; Cheng, R.; Sivadas, N.; Huang, B.; Schmidgall, E.; Taniguchi, T.; Watanabe, K.; McGuire, M. A.; Yao, W.; Xiao, D.; Fu, K.-M. C.; Xu, X. Van der Waals Engineering of Ferromagnetic Semiconductor Heterostructures for Spin and Valleytronics. *Sci. Adv.* **2017**, *3*, No. e1603113.

(25) Yang, A.; Blancon, J.-C.; Jiang, W.; Zhang, H.; Wong, J.; Yan, E.; Lin, Y.-R.; Crochet, J.; Kanatzidis, M. G.; Jariwala, D.; Low, T.; Mohite, A. D.; Atwater, H. A. Giant Enhancement of Photoluminescence Emission in WS_2-Two-Dimensional Perovskite Heterostructures. *Nano Lett.* **2019**, *19*, 4852−4860.

(26) Liu, W. J.; Liu, M. L.; Liu, B.; Quhe, R. G.; Lei, M.; Fang, S. B.; Teng, H.; Wei, Z. Y. Nonlinear Optical Properties of MoS_2-WS_2 Heterostructure in Fiber Lasers. *Opt. Express* **2019**, *27*, 6689−6699.

(27) McCreary, K. M.; Hanbicki, A. T.; Singh, S.; Kawakami, R. K.; Jernigan, G. G.; Ishigami, M.; Ng, A.; Brintlinger, T. H.; Stroud, R. M.; Jonker, B. T. The Effect of Preparation Conditions on Raman and Photoluminescence of Monolayer WS_2. *Sci. Rep.* **2016**, *6*, 35154.

(28) Fang, Y.; Wu, S.; Zhu, Z.-Z.; Guo, G.-Y. Large Magneto-optical Effects and Magnetic Anisotropy Energy in two-dimensional $Cr_2Ge_2Te_6$. *Phys. Rev. B* **2018**, *98*, 125416.
(29) Xing, W.; Chen, Y.; Odenthal, P. M.; Zhang, X.; Yuan, W.; Su, T.; Song, Q.; Wang, T.; Zhong, J.; Jia, S.; Xie, X. C.; Li, Y.; Han, W. Electric Field Effect in Multilayer $Cr_2Ge_2Te_6$: a Ferromagnetic 2D Material. *2D Mater.* **2017**, *4*, 024009.
(30) Zhang, L.; Yan, H.; Sun, X.; Dong, M.; Yildirim, T.; Wang, B.; Wen, B.; Neupane, G. P.; Sharma, A.; Zhu, Y.; Zhang, J.; Liang, K.; Liu, B.; Nguyen, H. T.; Macdonald, D.; Lu, Y. Modulated Interlayer Charge Transfer Dynamics in a Monolayer TMD/metal Junction. *Nanoscale* **2019**, *11*, 418−425.
(31) Gong, Y.; Lin, J.; Wang, X.; Shi, G.; Lei, S.; Lin, Z.; Zou, X.; Ye, G.; Vajtai, R.; Yakobson, B. I.; Terrones, H.; Terrones, M.; Tay, B. K.; Lou, J.; Pantelides, S. T.; Liu, Z.; Zhou, W.; Ajayan, P. M. Vertical and in-plane Heterostructures from WS_2/MoS_2 Monolayers. *Nat. Mater.* **2014**, *13*, 1135.
(32) Lin, Y.-C.; Ghosh, R. K.; Addou, R.; Lu, N.; Eichfeld, S. M.; Zhu, H.; Li, M.-Y.; Peng, X.; Kim, M. J.; Li, L.-J.; Wallace, R. M.; Datta, S.; Robinson, J. A. Atomically Thin Resonant Tunnel Diodes built from Synthetic Van Der Waals Heterostructures. *Nat. Commun.* **2015**, *6*, 7311.
(33) Yuan, L.; Huang, L. Exciton Dynamics and Annihilation in WS_2 2D Semiconductors. *Nanoscale* **2015**, *7*, 7402−7408.
(34) Xu, R.; Yang, J.; Zhu, Y.; Yan, H.; Pei, J.; Myint, Y. W.; Zhang, S.; Lu, Y. Layer-dependent Surface Potential of Phosphorene and Anisotropic/layer-Dependent Charge Transfer in Phosphorene−gold Hybrid Systems. *Nanoscale* **2016**, *8*, 129−135.
(35) Sharma, I.; Mehta, B. R. KPFM and CAFM based Studies of MoS_2 (2D)/WS_2 Heterojunction Patterns Fabricated Using Stencil Mask Lithography Technique. *J. Alloys Compd.* **2017**, *723*, 50−57.
(36) Melitz, W.; Shen, J.; Kummel, A. C.; Lee, S. Kelvin Probe Force Microscopy and its Application. *Surf. Sci. Rep.* **2011**, *66*, 1−27.
(37) Kaushik, V.; Varandani, D.; Mehta, B. R. Nanoscale Mapping of Layer-Dependent Surface Potential and Junction Properties of CVD-Grown MoS_2 Domains. *J. Phys. Chem. C* **2015**, *119*, 20136−20142.
(38) Wang, H.; Huang, C.-C.; Polcar, T. Triboelectrification of Two-Dimensional Chemical Vapor Deposited WS_2 at Nanoscale. *Sci. Rep.* **2019**, *9*, 334.
(39) Hao, G.; Kou, L.; Lu, D.; Peng, J.; Li, J.; Tang, C.; Zhong, J. Electrostatic Properties of two-dimensional WSe2 Nanostructures. *J. Appl. Phys.* **2016**, *119*, 035301.
(40) Ziegler, D.; Gava, P.; Güttinger, J.; Molitor, F.; Wirtz, L.; Lazzeri, M.; Saitta, A. M.; Stemmer, A.; Mauri, F.; Stampfer, C. Variations in the Work function of Doped single- and Few-layer Graphene Assessed by Kelvin Probe Force Microscopy and Density Functional Theory. *Phys. Rev. B: Condens. Matter Mater. Phys.* **2011**, *83*, 235434.
(41) Cai, Y.; Zhang, G.; Zhang, Y.-W. Layer-dependent Band Alignment and Work Function of Few-Layer Phosphorene. *Sci. Rep.* **2014**, *4*, 6677.
(42) Choi, S.; Shaolin, Z.; Yang, W. Layer-number-Dependent Work Function of MoS_2 Nanoflakes. *J. Korean Phys. Soc.* **2014**, *64*, 1550−1555.
(43) Sang, D. K.; Wang, H.; Qiu, M.; Cao, R.; Guo, Z.; Zhao, J.; Li, Y.; Xiao, Q.; Fan, D.; Zhang, H. Two Dimensional β-InSe with Layer-Dependent Properties: Band Alignment, Work Function and Optical Properties. *Nanomaterials* **2019**, *9*, 82.
(44) Tebyetekerwa, M.; Zhang, J.; Liang, K.; Duong, T.; Neupane, G. P.; Zhang, L.; Liu, B.; Truong, T. N.; Basnet, R.; Qiao, X.; Yin, Z.; Lu, Y.; Macdonald, D.; Nguyen, H. T. Quantifying Quasi-Fermi Level Splitting and Mapping its Heterogeneity in Atomically Thin Transition Metal Dichalcogenides. *Adv. Mater. (Weinheim, Ger.)* **2019**, *31*, 1900522.
(45) Tang, X.; Fan, D.; Peng, K.; Yang, D.; Guo, L.; Lu, X.; Dai, J.; Wang, G.; Liu, H.; Zhou, X. Dopant Induced Impurity Bands and Carrier Concentration Control for Thermoelectric Enhancement in p-Type $Cr_2Ge_2Te_6$. *Chem. Mater.* **2017**, *29*, 7401−7407.
(46) Ji, H.; Stokes, R. A.; Alegria, L. D.; Blomberg, E. C.; Tanatar, M. A.; Reijnders, A.; Schoop, L. M.; Liang, T.; Prozorov, R.; Burch, K. S.; Ong, N. P.; Petta, J. R.; Cava, R. J. A Ferromagnetic Insulating Substrate for the Epitaxial Growth of Topological Insulators. *J. Appl. Phys.* **2013**, *114*, 114907.
(47) Zhang, J.; Hong, H.; Zhang, J.; Fu, H.; You, P.; Lischner, J.; Liu, K.; Kaxiras, E.; Meng, S. New Pathway for Hot Electron Relaxation in Two-Dimensional Heterostructures. *Nano Lett.* **2018**, *18*, 6057−6063.
(48) Robert, C.; Semina, M. A.; Cadiz, F.; Manca, M.; Courtade, E.; Taniguchi, T.; Watanabe, K.; Cai, H.; Tongay, S.; Lassagne, B.; Renucci, P.; Amand, T.; Marie, X.; Glazov, M. M.; Urbaszek, B. Optical Spectroscopy of Excited Exciton States in MoS_2 monolayers in Van der Waals Heterostructures. *Phys. Rev. Mater.* **2018**, *2*, 011001.
(49) Karsthof, R.; von Wenckstern, H.; Zúñiga-Pérez, J.; Deparis, C.; Grundmann, M. Nickel Oxide−Based Heterostructures with Large Band Offsets. *Phys. Status Solidi B* **2020**, *257*, 1900639.
(50) Tisdale, W. A.; Williams, K. J.; Timp, B. A.; Norris, D. J.; Aydil, E. S.; Zhu, X. Y. Hot-Electron Transfer from Semiconductor Nanocrystals. *Science (Washington, DC, U.S.)* **2010**, *328*, 1543.
(51) Chu, W.; Saidi, W. A.; Zheng, Q.; Xie, Y.; Lan, Z.; Prezhdo, O. V.; Petek, H.; Zhao, J. Ultrafast Dynamics of Photongenerated Holes at a CH_3OH/TiO_2 Rutile Interface. *J. Am. Chem. Soc.* **2016**, *138*, 13740−13749.
(52) Chen, Z.; Zhang, Q.; Luo, Y. Experimental Identification of Ultrafast Reverse Hole Transfer at the Interface of the Photoexcited Methanol/Graphitic Carbon Nitride System. *Angew. Chem., Int. Ed.* **2018**, *57*, 5320−5324.
(53) Cirloganu, C. M.; Padilha, L. A.; Lin, Q.; Makarov, N. S.; Velizhanin, K. A.; Luo, H.; Robel, I.; Pietryga, J. M.; Klimov, V. I. Enhanced Carrier Multiplication in Engineered Quasi-type-II Quantum Dots. *Nat. Commun.* **2014**, *5*, 4148.
(54) He, J.; Ding, G.; Zhong, C.; Li, S.; Li, D.; Zhang, G. Remarkably Enhanced Ferromagnetism in a Super-exchange Governed $Cr_2Ge_2Te_6$ Monolayer via Molecular Adsorption. *J. Mater. Chem. C* **2019**, *7*, 5084−5093.
(55) Yu, Y.; Hu, S.; Su, L.; Huang, L.; Liu, Y.; Jin, Z.; Purezky, A. A.; Geohegan, D. B.; Kim, K. W.; Zhang, Y.; Cao, L. Equally Efficient Interlayer Exciton Relaxation and Improved Absorption in Epitaxial and Nonepitaxial MoS_2/WS_2 Heterostructures. *Nano Lett.* **2015**, *15*, 486−491.
(56) Zhuiykov, S. Electrons and holes in a semiconductor. In *Nanostructured Semiconductor Oxides for the Next Generation of Electronics and Functional Devices*; Zhuiykov, S., Ed.; Woodhead Publishing, 2014; pp 1−49.
(57) Nguyen, T. H.; O'Leary, S. K. The Dependence of the Fermi level on Temperature, Doping Concentration, and Disorder in Disordered Semiconductors. *J. Appl. Phys.* **2000**, *88*, 3479−3483.
(58) Jagtap, A. M.; Khatei, J.; Koteswara Rao, K. S. R. Exciton−phonon Scattering and Nonradiative Relaxation of Excited Carriers in Hydrothermally Synthesized CdTe Quantum Dots. *Phys. Chem. Chem. Phys.* **2015**, *17*, 27579−27587.
(59) Christopher, J. W.; Goldberg, B. B.; Swan, A. K. Long tailed Trions in Monolayer MoS_2: Temperature Dependent Asymmetry and Resulting Red-shift of Trion Photoluminescence Spectra. *Sci. Rep.* **2017**, *7*, 14062.
(60) Suzuki, M.; Gao, B.; Koshiishi, K.; Nakata, S.; Hagiwara, K.; Lin, C.; Wan, Y. X.; Kumigashira, H.; Ono, K.; Kang, S.; Kang, S.; Yu, J.; Kobayashi, M.; Cheong, S. W.; Fujimori, A. Coulomb-Interaction Effect on the Two-Dimensional Electronic Structure of the Van der Waals Ferromagnet $Cr_2Ge_2Te_6$. *Phys. Rev. B* **2019**, *99*, 161401.
(61) Li, Y. F.; Wang, W.; Guo, W.; Gu, C. Y.; Sun, H. Y.; He, L.; Zhou, J.; Gu, Z. B.; Nie, Y. F.; Pan, X. Q. Electronic Structure of Ferromagnetic Semiconductor $CrGeTe_3$ by angle-resolved Photoemission Spectroscopy. *Phys. Rev. B* **2018**, *98*, 125127.
(62) Su, J.; Wang, M.; Liu, G.; Li, H.; Han, J.; Zhai, T. Air-Stable 2D Intrinsic Ferromagnetic Ta_3FeS_6 with Four Months Durability. *Adv. Sci.* **2020**, *7*, 2001722.
(63) Huang, Y.; Sutter, E.; Shi, N. N.; Zheng, J.; Yang, T.; Englund, D.; Gao, H.-J.; Sutter, P. Reliable Exfoliation of Large-Area High-

https://dx.doi.org/10.1021/acsami.0c20110
ACS Appl. Mater. Interfaces 2021, 13, 7423−7433

Quality Flakes of Graphene and Other Two-Dimensional Materials. *ACS Nano* **2015**, *9*, 10612−10620.
(64) Xie, L.; Guo, L.; Yu, W.; Kang, T.; Zheng, R.-K.; Zhang, K. Ultrasensitive Negative Photoresponse in 2D $Cr_2Ge_2Te_6$ Photodetector with Light-Induced Carrier Trapping. *Nanotechnology* **2018**, *29*, 464002.
(65) Pei, J.; Yang, J.; Xu, R.; Zeng, Y.-H.; Myint, Y. W.; Zhang, S.; Zheng, J.-C.; Qin, Q.; Wang, X.; Jiang, W.; Lu, Y. Exciton and Trion Dynamics in Bilayer MoS_2. *Small* **2015**, *11*, 6384−6390.

https://dx.doi.org/10.1021/acsami.0c20110
ACS Appl. Mater. Interfaces 2021, 13, 7423−7433